

Depth-Sensing using AFM Contact-Resonance Imaging and Spectroscopy at the Nanoscale

C. Ma,^{1, a)} W. Wang,¹ Y. Chen,^{1, b)} W. Arnold,² and J. Chu¹

¹⁾*Department of Precision Machinery and Precision Instrumentation, University of Science and Technology of China, Hefei 230026, China*

²⁾*Department of Materials Science and Engineering, Saarland University, D-66123 Saarbrücken, Germany*

(Dated: 16 AUG 2019)

Subsurface metrology techniques are of significant importance at the nanoscale, for instance for imaging buried defects in semiconductor devices and in intracellular structures. Recently, ultrasonic-based atomic force microscopy has attracted intense attention, also for subsurface imaging. Despite many applications for measuring the real and imaginary part of the local surface modulus, the physical mechanism for subsurface imaging is not fully understood. This prevents accurate data interpretation and quantitative reconstruction of subsurface features and hinders the development of an optimized experimental and engineering set-up. In this paper, we present quantitative depth-sensing of subsurface cavity structures using contact-resonance atomic force microscopy (CR-AFM) imaging and spectroscopy. Our results indicate that for imaging subsurface cavity structures using CR-AFM the induced contact stiffness variations are the key contrast mechanism. **The developed algorithm based on this mechanism allows to precisely simulate the experimental image contrasts and give accurate prediction of the detection depth. The results allow a better understanding of the imaging mechanism of ultrasonic-based AFM and pave the way for quantitative subsurface reconstruction.**

Keywords: subsurface imaging, ultrasonic atomic force microscopy, contact resonance, cavity, quantitative reconstruction

I. INTRODUCTION

In non-destructive testing **and evaluation** subsurface metrology and imaging are important tools for detecting defects in components and products. **This** also holds for products and manufacturing processes where nanoscale properties become important, e.g. for wafers, in microelectronic devices, for thin films, and in biological structures. Besides microfocal X-ray imaging, optical and infrared techniques, ultrasonic techniques are in widespread use. Optical imaging systems are limited in resolution due to diffraction in the sub-micrometer range. In case of ultrasound, there is an indirect limitation for employing sub-micrometer wavelengths because of scattering in the component to be tested and above all due to the attenuation in the coupling medium water of the acoustic lens. This caused an upper limit of about 2 GHz for a practical scanning acoustic microscope (SAM)¹ (resolution \approx wavelength $\lambda \approx 0.75 \mu\text{m}$) despite considerable efforts to find other coupling media with lower attenuation. Using a low-temperature SAM operated at 8 GHz **with** superfluid helium as a coupling medium in order to achieve both a short **wavelength and low** attenuation, a resolution down to 20 nm has been **demonstrated**.² Due to the lack of practical coupling media besides **water, commercial** SAMs are operated at frequencies between 10 and 100 MHz.³ Near-field **microscopes** based on apertures or tips as antennas may be used instead. Here, the

technological challenge arises whether submicron resolution can be combined with depth resolution besides clarifying **the contrast** mechanism.

Combinations of an aperture with an acoustic lens were designed by Dürr *et al.*⁴ and Khuri-Yakub *et al.*⁵. A scanning near-field acoustic microscope using a pin was built by Zienuk and Latuszek⁶ with a resolution of 10 μm at 35 MHz. Furthermore, Kulik *et al.*⁷ developed a continuous wave (CW) system, where the reflection amplitude of a CW signal at a frequency of 1 MHz propagating in a tapered horn was used as contrast quantity. The resolution was determined by the horn diameter of 100 μm . **In a set-up built by** Güthner *et al.*⁸, **the** sharp corner of a vibrating tuning fork acted as a tip. **Friction within** the moving air between tip and surface determined the contrast. The spatial resolution was better than 3 μm .

Therefore, it was natural to combine the near-field imaging principles of scanning tunneling **microscopy or** atomic force microscopy (AFM) with ultrasonics. Indeed Heil *et al.*⁹, Takata *et al.*¹⁰, Uozumi and Yamamuro¹¹, Khuri-Yakub *et al.*¹², Chilla *et al.*¹³, and Moreau and Ketterson¹⁴ developed instruments which combined ultrasonics with a tunneling microscope, using the sharp tip as antenna. Resolution below 0.1 μm was thus achieved. The contrast mechanisms for imaging were not discussed in detail in these early papers, **with the exception** that the acoustic impedance or the tunneling current were involved. With the advent of atomic force microscopy, efforts concentrated on combining AFM and ultrasonics because AFMs were available commercially early on, and in particular allowed not only to study metals but also insulating materials.

^{a)}Electronic mail: chfuma@ustc.edu.cn

^{b)}Electronic mail: chenylh@ustc.edu.cn

Since the first introduction of ultrasonic force **microscopes two decades ago**^{15,16}, quite a number of related **instrument techniques** have been developed, see for example the **articles in** “*Acoustic Scanning Probe Microscopy*”¹⁷ **and** the references contained therein. The research efforts first concentrated deriving quantitatively the local elastic and anelastic modulus from the measured **contact stiffness**.^{18,19} The spatial resolution was given by the tip-sample contact radius a_c , which is a fraction of the tip radius R , **and can** be as small as a few nanometers.

Soon the question arose whether there was the possibility performing subsurface imaging, because the elastic stress-field generated by the tip in a homogeneous body extends to about $3a_c$ into the depth²⁰, altering the contact stiffness if defects were present. Indeed it was shown that there is subsurface contrast, see the articles of Avasthy *et al.*, Cantrell and Cantrell, Kolosov and Briggs, Parlak and Degertekin, Yamanaka and Tsuji, and Vairac *et al.* in¹⁷ and the articles cited therein. There is early work by Scherer *et al.*²¹ and further detailed work by Striegler *et al.*²² and Verbiest *et al.*^{23,24}.

In these references, the contrast mechanism for subsurface imaging is discussed, sometimes quite controversial. Two points of views prevail: (i) contrast due to scattering of ultrasonic waves in the near field^{25,26} and (ii) contrast due to changes in the contact stiffness^{16,22,26–34}. Moreover, it has been suggested that both mechanisms contribute to the image contrast²⁶ and that variations of contact stiffness and the viscoelastic damping of the subsurface structure, here gold particles of 40 nm diameters, contribute to the contrast^{34,35} or that solely interfacial friction of the oscillating gold nanoparticles in the polymer material causes the contrast.²⁴ In the model of Cantrell and Cantrell in¹⁷ the contrast is determined by the static tip load, the contact stiffness, and the contact damping. These parameters are modified by subsurface cavities and inclusions.

In this work, we present imaging and spectroscopy data of subsurface cavities using AFM contact-resonances and employing different flexural cantilever modes, thus extending our previous work³⁶. Our results show that it is sufficient to invoke contact stiffness variations as the key physical contrast mechanism for subsurface cavity **structures**.

II. EXPERIMENTAL METHODS

A. Contact-Resonance Imaging and Spectroscopy

A schematic illustration of contact-resonance (CR) measurements for subsurface imaging is shown in Fig. 1a. A silicon substrate with holes covered by an HOPG (**highly oriented pyrolytic graphite**) flake is scanned with an AFM in contact mode. The excitation of the cantilever contact-resonances is achieved either by a piezo-element built in the cantilever holder (**ultrasonic atomic force microscopy**, UAFM) or by a transducer attached

to the backside of the sample (**atomic force acoustic microscopy**, AFAM). For the detection and the display of the cantilever vibrations, the instrument's photo-diode and its amplifier circuit are used. Such measurements are operated in two modes. In the spectroscopy mode, a cantilever amplitude spectrum is obtained by sweeping the excitation frequency of the transducer or of the cantilever holder's piezo-element at each measuring point. In the imaging mode, the cantilever is excited at a close frequency or at the contact-resonance frequency while mapping the sample. For demonstrations, we show in Fig. 1b cantilever spectra measured on the Si substrate and on the HOPG flake. The spectra display the first three flexural resonances of the cantilever which exhibit frequency shifts that depend on whether the AFM tip contacts the Si surface or the HOPG flake. Figure 1c shows the AFM topography and CR-AFM amplitude images acquired near a HOPG flake. The subsurface holes covered by the HOPG flake are clearly visible in the amplitude image.

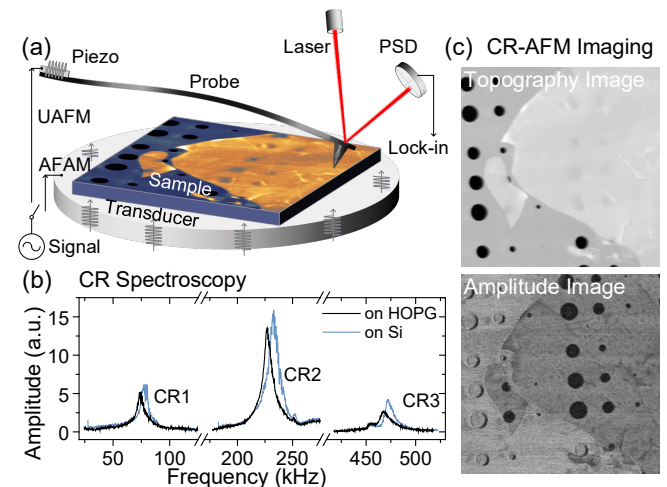


FIG. 1. (a) Schematic illustration of CR-AFM scans on a HOPG flake covering open holes on a Si substrate; (b) Vibration spectra on the HOPG flake and on the Si substrate for the first three flexural eigenmodes of the AFM probe; (c) AFM topography and CR-AFM amplitude image.

In our experiments, UAFM images were obtained with a MFP-3D Origin AFM (Asylum Research, Santa Barbara, CA). AFAM mode experiments were carried out with a Dimension Icon (Bruker, Santa Barbara, CA). A commercial transducer (Steiner & Martins Inc., FL) was used to excite the CRs. Furthermore, all CR spectroscopy measurements were carried out with the AFAM mode. The cantilevers used were Multi75-G and ContA1-G probes from Budget-Sensors, Bulgaria, with spring constants k_c of respectively 3.10 and 0.31 N/m. The spring constants were measured using the well-known thermal method yielding also the free resonance frequencies for the first flexural mode of the two probes: 75.6 and 14.6 kHz.

B. Sample Preparation

By electron-beam lithography holes were fabricated in a pattern-like arrangement into the silicon wafers. Each pattern contained nine holes of approx. 155 nm depth determined by AFM. The data showed that they are hardly tapered. Their diameters are 178 ± 12 , 424 ± 7 , 615 ± 13 , 821 ± 12 , 1116 ± 15 , 1313 ± 24 , 1521 ± 17 , 1714 ± 12 , and 1927 ± 22 nm, as measured by scanning electron microscopy (SEM) (EVO 18, ZEISS). Using the scotch-tape method, freshly cleaved HOPG flakes with thicknesses of 25, 110, 247, and 392 nm were transferred onto the Si substrate partially covering the hole pattern. The thicknesses of the HOPG flakes were measured by AFM height profiles. Measurements at five different locations gave standard deviations of maximal 3 nm for all the flakes. **Although cavities may have various shapes and at different depths, such samples can be used in order to clarify the subsurface imaging contrast without loss of generality.**

C. Cantilever Dynamics and Contact Mechanics

In CR-AFM, by using proper models for the cantilever vibrations and contact mechanics, the data are analyzed in a two-step process. In a first step the tip-sample contact stiffness is obtained, followed by a second step in order to obtain the sample's indentation modulus with a spatial resolution given by the contact radius.^{19,37–42}

To relate the measured CR frequency with the contact stiffness, the oscillatory behavior of cantilever was modeled taking into account the tip position, the cantilever tilt, and the lateral contact stiffness. The contact damping was neglected. A detailed description of the model can be found elsewhere³⁷. The parameters of the employed Multi75-G probe were: cantilever length $L = L_1 + L_2 = 225 \mu\text{m}$, cantilever tilt $\alpha_0 = 11$, tip height $h = 17 \mu\text{m}$, tip position $L_1 = 215 \mu\text{m}$, and ratio between the normal and lateral contact stiffness $\tau = k_L/k_N = 0.85$, see Fig. 2a.

In the case of scanning the HOPG flake above a cavity (Fig. 2b), the normal tip-sample contact stiffness k_N is regarded as a series connection of the stiffness k_S of the cavity structure and of the material stiffness k_M .

$$\frac{1}{k_N} = \frac{1}{k_M} + \frac{1}{k_S} \quad (1)$$

When the tip is far away from the cavity in the supported HOPG flake region (Fig. 2c), k_S becomes infinite, and hence $k_N = k_M$. Considering a Hertzian contact, k_M is determined by the tip radius R and the applied tip load F_N :

$$k_M = (6E^*2RF_N)^{1/3} \quad (2)$$

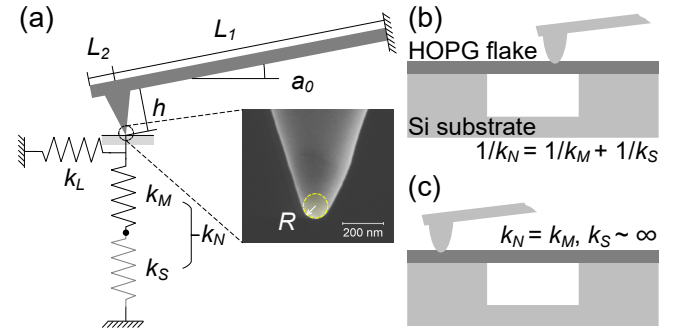


FIG. 2. (a) Cantilever model taking into account the tip position and the lateral contact stiffness of the tip-sample contact. Inset: SEM image of the tip of the Multi75-G probe taken after measurements; (b) and (c) illustrations of the tip contacting on top of a cavity and on the supported HOPG flake. The normal contact stiffness k_N on top of the cavity is represented by a series connection of the deflection stiffness k_S and the material stiffness k_M .

Here, E^* is the reduced Young's modulus with $1/E^* = (1 - \nu_t^2)/E_t + (1 - \nu_s^2)/E_s$ where (E_t, ν_t) and (E_s, ν_s) are respectively the Young's modulus and the Poisson's ratio of the tip and the sample. It should be mentioned that the effect of the Si substrate on the effective elastic modulus of the HOPG flake is omitted in the calculations which follow. The ensuing error can be estimated using the theory of Perriot and Barthel⁴³, allowing **one** to calculate the stiffness of coated half-spaces. This produces approx. 18.3%, 4.1%, 1.4%, and 1.1% lower values for k_M for flake thicknesses of respectively 25, 110, 247, and 392 nm. The analysis was made using a contact radius of 10.8 nm corresponding to a tip radius of 100 nm and a tip load of 300 nN. For the smaller contact radii in our experiments, the substrate effect will be smaller. **Finally, we observe no signs of heterogeneous adhesion between the HOPG flake and the Si substrate.**

The part of the HOPG flake covering the holes of the Si wafer is considered to be an edge-clamped circular free-standing membrane with a diameter of $2r_0$ and a thickness of t . For such a membrane with a point force P attacking at a distance of r from its center, the stiffness is given by:⁴⁴

$$k_S = \frac{16\pi D r_0^2}{(r_0^2 - r^2)^2} \quad (3)$$

where $D = E_s t^3 / (12(1 - \nu_s^2))$ is the flexural plate rigidity. In our analyses, a Young's modulus and a Poisson's ratio of (169 GPa, 0.27) and (18 GPa, 0.25) were respectively used for the Si tip and the HOPG sample. Furthermore, after all the measurements reported here, the tip for the employed Multi75-G probe was examined by using a cold field emission SEM (SU8220, Hitachi) with a magnification of 50000 \times . As seen in the inset of Fig. 2a, the tip shape is spherical **with a radius $R = 68$ nm.** **Fresh AFM tips wear during scanning in contact mode**

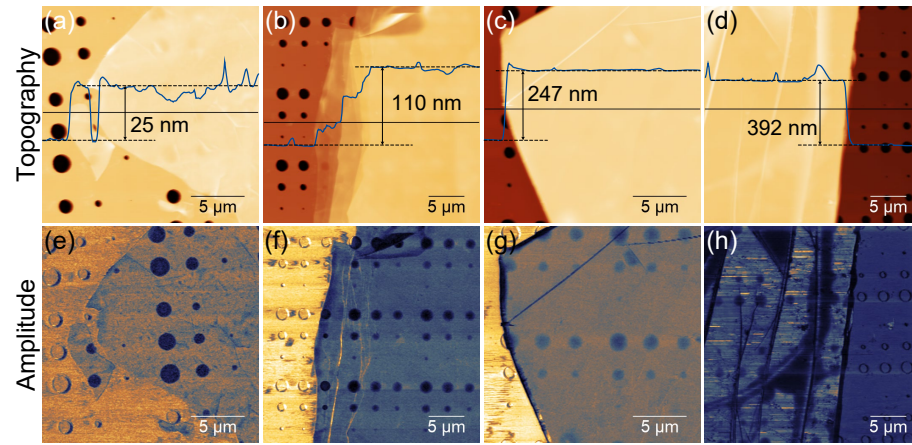


FIG. 3. (a) - (d) Topography and (e) - (h) corresponding UAFM amplitude images taken on the HOPG flakes. Some of the holes were not covered and became visible in the topography images as well. The line scans shown in (a) - (d) and obtained by scanning over the edge of the flakes indicate their thicknesses: (a) 25, (b) 110, (c) 247, and (d) 392 nm. The UAFM experiments were made using the first CR resonance, which is close to 410 kHz on Si for an applied load of approx. 210 nN exerted by the Multi75-G cantilever.

when large contact forces are applied. In turn, deliberate but controlled tip-wear when scanning a Si substrate prior to CR-AFM, results in defined and stable tip shapes for further measurements.

III. RESULTS AND DISCUSSION

A. Depth-sensing using CR-AFM

We first describe the sensitivity of CR-AFM imaging for subsurface cavities at various depths. UAFM imaging was performed on four HOPG flakes with thicknesses of 25, 110, 247, and 392 nm using the Multi75-G cantilever. All experiments were carried out at the first flexural CR of the cantilever close to 410 kHz on the Si substrate with an applied load of 210 nN. The resulting topography and the corresponding UAFM amplitude images are shown in Figs. 3a-3d and Figs. 3e-3h. In contrast to the topography images, the amplitude images clearly reveal the subsurface cavities. Furthermore, with increasing flake thickness, the contrast of the cavities becomes gradually weaker. While the smallest cavities can still be distinguished below the thinnest flake, only cavities with large diameters can be detected and spatially resolved when scanning the 392 nm thick flake.

For a quantitative study, we determine the modulation contrast M of the subsurface cavities displayed in Fig. 3:

$$M = \frac{A_{sub} - A_{cav}}{A_{sub} + A_{cav}} \quad (4)$$

where A_{sub} and A_{cav} stand for the amplitudes measured on HOPG flakes far away and at the surface centers of the cavities. The results are shown in Fig. 4a. An overall decrease of the contrast can be clearly seen for

deeper and smaller cavities. It can also be seen that for a flake thickness of 25 nm, all cavities can be detected. However, for cavities covered by HOPG flakes with thicknesses of 110, 247, and 392 nm, the contrast for cavity diameters smaller than 424, 615, and 1116 nm is not sufficient, so that they no longer can be detected with our experimental system.

To explain the observed image contrast, we analyze how the subsurface features influence contact stiffness and hence CR frequencies. When the tip is above the cavity the contact stiffness is regarded as a series connection (Fig. 2b) given by Eq. 1 and for the contact stiffness on the supported HOPG flake region given by Eq. 2. For the Multi75-G cantilever used, we calculate and display in Fig. 4b the dispersion curves for the first and second flexural cantilever modes, which relate the CR frequency to the contact stiffness k_N . For a tip load $F_N = 210$ nN for the tip with a radius of $R = 68$ nm, the contact stiffness on the supported HOPG flake is $k_M = 296$ N/m according to Eq. 2. For the first mode the corresponding CR frequency is 366.4 kHz (Fig. 4b). For our measurement setup, a CR frequency resolution of $\Delta f_c = 1.0$ kHz is considered, which corresponds to a minimum modulation threshold of $M \approx 0.02$ for amplitude images for a quality factor of 50. Thus, when scanning, cavities can only be discerned, if the sensed contact stiffness at their centers are smaller than $k_N = 289$ N/m.

For a number of cavities with varying diameters and depths, the contact stiffness k_N at their surface centers was calculated using Eqs. 1 - 3. The background color of Fig. 4c corresponds to k_N with the color scale displayed at its side. The contour line for $k_N = 289$ N/m separates the detectable from the non-detectable cavities depending on their diameters and depths. The detectability of the cavities in Fig. 3 can be easily seen by overlaying them with their diameters and depths onto Fig. 4c.

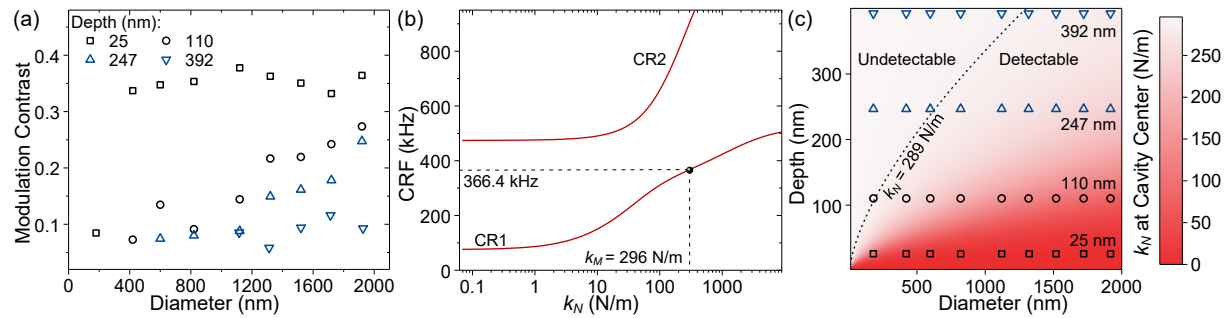


FIG. 4. (a) Modulation contrast M as a function of diameter of the cavities with the flake thickness as a parameter; (b) dispersion curve for the CR frequency of the Multi75-G cantilever as a function of the normal contact stiffness k_N for the first two eigenmodes; (c) calculated normal contact stiffness k_N at the cavity's center for various diameters and depths for a tip radius $R = 68$ nm and a tip load of $F_N = 210$ nN. The dashed lines in (b) represent the contact stiffness on the supported HOPG flake region $k_M = 296$ N/m and the corresponding CR frequency 366.4 kHz. The contour line in (c) indicates the threshold contact stiffness $k_N = 289$ N/m using the first CR mode.

B. Image Contrast

The oscillation of an AFM cantilever can be separated into a mode-shape part and a time-dependent part. The time-dependent part of the cantilever oscillation in the tip-sample contact can be described as a driven damped harmonic oscillator with a Lorentzian resonance line-shape for the amplitude:

$$A(f_{exc}) = A_{peak} \frac{1}{\sqrt{Q^2(1 - (\frac{f_{exc}}{f_c})^2)^2 + (\frac{f_{exc}}{f_c})^2}} \quad (5)$$

Here, A_{peak} is the peak amplitude at the resonance, f_c is the contact-resonance frequency which depends on the contact stiffness (see dispersion curves in Fig. 4b), f_{exc} is the excitation frequency, and Q is the quality factor. As an example we show in Fig. 5a the simulated CR spectra on the supported HOPG flake region and at the surface centers of the nine cavities examined with the Multi75-G cantilever for a tip load of 293 nN. For convenience, the amplitude was normalized so that $A_{peak} = 1$. Gradual shifts of the resonance to lower frequencies can be seen from the supported region to the largest cavity surface center. A constant quality factor $Q = 50$ was used in our calculations which is close to the measured value. The contact stiffness and the modal shape of the cantilever oscillations also influence the Q-value⁴⁵, however to a minor extent and hence it is neglected.

The operation frequency affects the contrast of amplitude images in CR-AFM^{22,46}. Therefore, in order to verify this aspect of the model, AFAM images with different excitation frequencies f_{exc} near the first CR frequency were obtained on a 125 nm thick HOPG flake for the Multi75-G cantilever with a tip load of 293 nN. A topography image of the flake and its adjacent area on the Si wafer are shown in Fig. 5b and the corresponding AFAM amplitude image at the excitation frequency $f_{exc} = 350$ kHz is shown in Fig. 5c. In this figure, the subsurface

cavities and also some other features related to the topography can be seen. More interesting is the contrast behavior of the cavities. Figure 5d shows the AFAM amplitude images taken on the encased area shown in Fig. 5c for $f_{exc} = 370, 360, 345, 330$, and 315 kHz. For $f_{exc} = 370$ kHz close to the CR on the supported HOPG flake region, all cavities appear darker than the supported region. When lowering f_{exc} stepwise towards 315 kHz, a frequency close to the CR at the surface center of the largest cavity, contrast reversals in the images of the cavities can be observed. Bright halos surround the cavity images which contract towards their centers with decreasing f_{exc} . This can be understood by the decrease of the contact stiffness causing also a decrease of the resonance frequency from the cavity peripheries to their centers. The simulated amplitude images for the corresponding frequencies are shown in Fig. 5e. Their appearance and contrast changes are quite close to the experimentally observed behavior. This is a strong hint that the contact stiffness is the main origin of CR-AFM for imaging subsurface cavities.

C. Depth Sensitivity

The sensitivity df_c/dk_N of the AFM cantilever to variations of the contact stiffness depends on the excited mode⁴². Let us give an example when using the ContAl-G cantilever with a tip of radius $R = 100$ nm and a tip load of 100 nN. A contact stiffness of 263 N/m is then obtained on the supported HOPG flake region considering a Hertzian contact (Eq. 2). For this set of contact stiffness, the modal sensitivities of the cantilever df_c/dk_N are determined to be approx. 0.03, 0.06 and 0.21 kHz/(N/m) for respectively the first three flexural modes. For similar experimental set-ups, the stiffness sensitivity is expected to get better for the higher modes. This opens the possibility to exploit different modes for sensing subsurface structures at different depths, which has been exploited

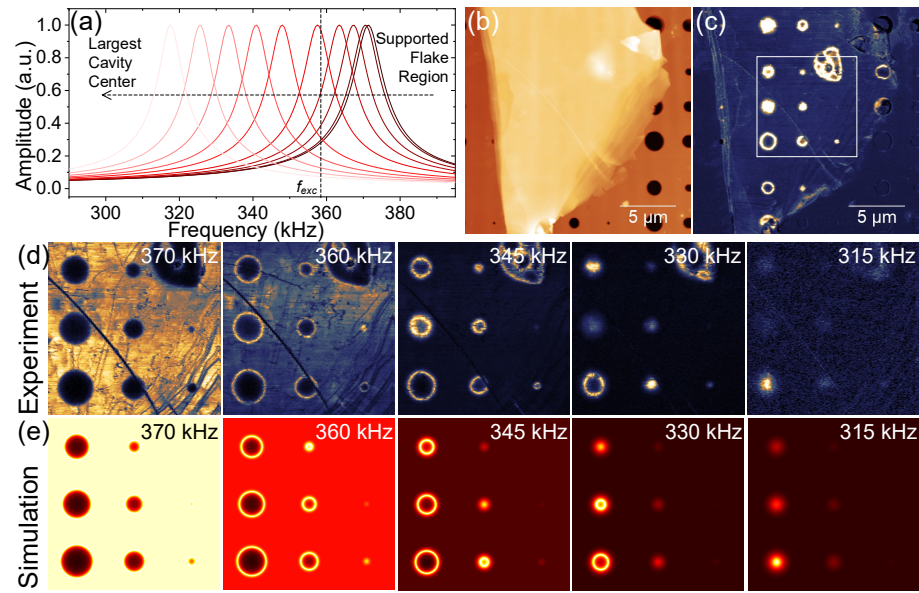


FIG. 5. (a) simulated CR spectra on the supported HOPG flake region and at the centers of the nine subsurface cavities. The cantilever oscillations represent a driven damped harmonic oscillator with a quality factor $Q = 50$; (b) Topography and (c) AFAM amplitude image on a HOPG flake with a thickness of 125 nm using the Multi75-G cantilever operated at frequency of 350 kHz and for a tip load of 293 nN; (d) AFAM amplitude images of the encased area in (c) for various operating frequencies; (e) simulated amplitude images for the operating frequencies used for (d).

for subsurface detection of stiff particles in a polymer³⁰.

Here, we demonstrate this possibility by conducting UAFM imaging on a HOPG flake using the first three modes of the ContA1-G probe. The flake has a thickness of 81 nm. A tip load of 95 nN was applied, and the operating frequencies were chosen respectively as 70, 233, and 473 kHz close to the first three CR modes as shown in Fig. 1b. The resulting UAFM images are shown in Figs. 6a - 6c. At first sight, a better contrast of the cavities can be seen for the higher modes. This is confirmed by the modulation contrast values M obtained for the first three modes at the surface centers of the largest cavity feature, which are respectively around 0.09, 0.16, and 0.38. While with the first mode one can reveal some large cavities only blurrily, the second and the third modes allow to image the smaller cavities (see arrows) with good contrast. Furthermore, it can be seen that the first mode is more sensitive to surface features on the HOPG flake. The dashed lines indicate grain boundaries which were previously observed also with other approaches^{47,48}. The second and third modes however, show little indications on the surface but mainly subsurface features instead. Compared to the second mode's clean contrast on the supported HOPG flake region, the third mode image shows fluctuations on these areas which may come from fluctuated bonding strengths between the flake and the Si substrate. Although one can image and distinguish subsurface features under different depths by exploiting multiple eigenmodes, issues like mechanical cross-coupling from shallower planes renders tomography with a high depth resolution difficult to realize.

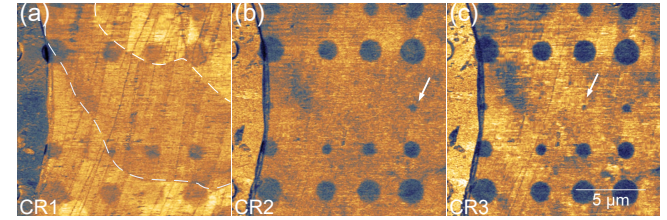


FIG. 6. UAFM amplitude images of a HOPG flake with a thickness of 81 nm using (a) the first (70 kHz); (b) the second (233 kHz); and (c) the third CR mode (473 kHz) of the ContA1-G probe for a tip load of 95 nN.

D. Reconstruction by CR Spectroscopy

In order to realize quantitative reconstruction of the geometry of the subsurface cavities, CR spectroscopy measurements were carried out for the largest cavity under the HOPG flake with a thickness of 125 nm. Again the Multi75-G cantilever was used with an applied tip load of 212 nN. The AFAM amplitude image of the cavity obtained at 380 kHz is shown in Fig. 7a. CR spectra were then recorded at 25 positions along its radial axis as illustrated in Fig. 7a. The spectra obtained at the right side of the cavity center are displayed in Fig. 7b. There is a gradual shift of the resonance from higher to lower frequencies when moving the tip towards the surface center of the cavity. This is in line with our analysis that the tip senses a contact stiffness decrease from the periphery to the center of the subsurface cavity. Interestingly, an increase of the resonance amplitude and the

This is the author's peer reviewed, accepted manuscript. However, the online version of record will be different from this version once it has been copyedited and typeset.
PLEASE CITE THIS ARTICLE AS DOI: 10.1063/1.5113567

quality factor can also be observed from the periphery to the cavity center. This is contrary to the fact that a lower resonance frequency will lead to a smaller quality factor due to the modal damping effect for the same local damping⁴⁵. This could be explained by a decreasing dissipation as a function of contact volume from the HOPG flake's supported region to the cavity center. The local damping factors Q^{-1} are determined from our data to be approx. 0.09 on the flake's supported region and 0.04 above the cavity center. Q^{-1} was calculated by modeling the tip-sample contact as a Kelvin-Voigt element and describing the cantilever's motion with a complex wave vector. In this way, the modal effect and the air damping are considered and deducted. A complex contact stiffness $k^* = k_r + ik_i$ is then obtained with k_r and k_i being respectively the real and imaginary parts yielding the local damping factor by $Q^{-1} = k_i/k_r$.⁴⁵

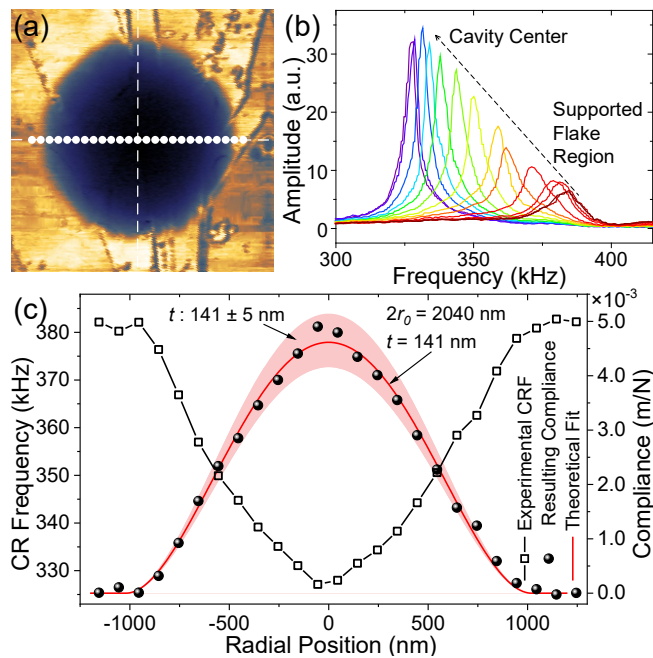


FIG. 7. (a) AFAM amplitude image of the largest cavity under a 125 nm thick HOPG flake. Scan size: $2.5 \times 2.5 \mu\text{m}^2$; (b) CR spectra acquired as a function of radial position as illustrated in (a) (only the right half side); (c) measured CR frequency and bending compliance along a radial axis through the cavity center. A theoretical fit of the bending compliance along the radial axis is also shown. The working frequency in (a) was 380 kHz. All experimental data were obtained for a tip load of 212 nN using the Multi75-G cantilever.

The CR frequencies along the radial axis are shown in Fig. 7c. A gradual decrease of the CR frequency can be seen from a value of near 382 kHz on the supported flake region to 327 kHz above the cavity center. From the dispersion curve of the cantilever (Fig. 4b), the corresponding contact stiffness k_N sensed by the tip can be acquired. Afterwards, the deflection stiffness k_S at those test points can be calculated using Eq. (1). The data are shown in Fig. 7c as its inverse counterpart, the bending

compliance $(1/k_S)$ ⁴⁹. Using Eq. 3 and taking the diameter $2r_0$ and the depth t as variables, we performed a least-square fit of the compliance data. The best-fit is shown in Fig. 7c as a solid line (in red) which yields a diameter of $2r_0 = 2040$ nm and a depth of $t = 141$ nm. Since the bending compliance is more sensitive to the variable depth than the variable diameter, an error band obtained by the fit is also shown in Fig. 7c for depths of $t \pm \Delta t = 141 \pm 5$ nm (shaded red area). Considering the measured diameter of the largest cavity (1927 nm) and the thickness of the flake (125 nm), the fits yield errors of approx. 6% and 13%.

IV. CONCLUSIONS

We presented contact-resonance AFM imaging and spectroscopy data for quantitative depth-sensing of subsurface nanoscale cavities. Based on contact stiffness changes, an algorithm has been developed to calculate the contrast of subsurface structures for CR-AFM images allowing also to reconstruct the depth and the lateral dimension of the subsurface cavities. In addition, tomography using CR-AFM seems possible by using multi-mode imaging. Our results support that contact stiffness variations are the key contrast mechanism for ultrasonic CR-AFM imaging of subsurface cavities. Furthermore, our experiments and modeling work show clearly that a number of parameters determine whether a subsurface cavity becomes detectable, and there is no simple rule of thumb for the depth sensitivity. This will also hold for stiff inclusions in a host material of given elasticity⁵⁰. In a related study, it has been shown that the concept for subsurface contrast discussed in this paper can also be applied for an AFM operated in the tapping mode.⁵¹

Note added after review process: We became aware that a paper on a similar subject has been accepted for publication in the journal “Nanoscale” by K. Yip, T. Cui, Y. Sun and T. Filleter, DOI: 10.1039/C9NR03730F.

ACKNOWLEDGMENTS

This work was financially supported by the National Natural Science Foundation of China (Reference No. 51675504). We thank W. Zhang for help on sample fabrication. We are grateful for the support of our research by allocating us resources of the USTC Center for Micro- and Nanoscale Research and Fabrication.

¹C. F. Quate, A. Atalar, and H. K. Wickramasinghe, *P. IEEE*, **67**, 1092 (1979).

²B. Hadimioglu and J. S. Foster, *J. Appl. Phys.*, **56**, 1976 (1984).

³R. S. Gilmore, K. C. Tam, J. D. Young, and D. R. Howard, *Phil. Trans. R. Soc. Lond. A*, **320**, 215 (1986).

⁴W. Dürr, D. A. Sinclair, and E. A. Ash, *Electron. Lett.*, **16**, 805 (1980).

This is the author's peer reviewed, accepted manuscript. However, the online version of record will be different from this version once it has been copyedited and typeset.

PLEASE CITE THIS ARTICLE AS DOI: 10.1063/1.5113567

- ⁵B. T. Khuri-Yakub, C. Cinbis, C. H. Chou, and P. A. Reinholdt-sen, in *Proc., IEEE Ultrasonics Symposium* (Montreal, 1989), pp. 805-807.
- ⁶J. K. Zienuk and A. Latuszek, in *Acoustical Imaging*, edited by H. Shimizu, N. Chubachi, and J. Kushibiki (Plenum Press, New York, 1989), pp. 219-224.
- ⁷A. Kulik, J. Attal, and G. Gremaud, in *Acoustical Imaging*, edited by Y. Wei and B. Gu (Plenum Press, New York, 1993), pp. 241-244.
- ⁸P. Güthner, U. C. Fischer, and K. Dransfeld, *Appl. Phys. B*, **48**, 89 (1989).
- ⁹J. Heil, J. Wesner, and W. Grill, *J. Appl. Phys.*, **64**, 1939 (1988).
- ¹⁰K. Takata, T. Hasegawa, S. Hosaka, S. Hosoki, and T. Komoda, *Appl. Phys. Lett.*, **55**, 1718 (1989).
- ¹¹K. Uozumi and K. Yamamuro, *Jpn. J. Appl. Phys.*, **28**, L1297 (1989).
- ¹²B. T. Khuri-Yakub, S. Akamine, B. Hadimioglu, H. Yamada, and C. F. Quate, in *Proc. SPIE 1556, Scanning Microscopy Instrumentation*, (San Diego, 1991), pp. 30-39.
- ¹³E. Chilla, W. Rohrbeck, H. J. Fröhlich, R. Koch, and K. H. Rieder, *Appl. Phys. Lett.*, **61**, 3107 (1992).
- ¹⁴A. Moreau and J. B. Ketterson, *J. Appl. Phys.*, **72**, 861 (1992).
- ¹⁵U. Rabe and W. Arnold, *Appl. Phys. Lett.*, **64**, 1493 (1994).
- ¹⁶K. Yamanaka, H. Ogiso, and O. Kolosov, *Appl. Phys. Lett.*, **64**, 178 (1994).
- ¹⁷F. Marinello, D. Passeri, E. Savio (Eds.), *Acoustic Scanning Probe Microscopy*, (Springer, Heidelberg, 2013).
- ¹⁸U. Rabe, in *Applied Scanning Probe Microscopy II*, edited by B. Bhushan and H. Fuchs, (Springer, Heidelberg, 2006), pp. 37-90.
- ¹⁹P. A. Yuya, D. C. Hurley, and J. A. Turner, *J. Appl. Phys.*, **104**, 074916 (2008).
- ²⁰K. L. Johnson, *Contact Mechanics*, (Cambridge University Press, Cambridge, 1985).
- ²¹V. Scherer, K. Janser, U. Rabe, W. Arnold, and O. Meissner, in *Rev. QNDE*, **16**, edited by D. O. Thompson and D. E. Chimenti, (Plenum Press, New York, 1997), pp. 1391-1398.
- ²²A. Striegler, B. Koehler, B. Bendjus et al., *Ultramicroscopy*, **111**, 1405 (2011).
- ²³G. J. Verbiest, T. H. Oosterkamp, and M. J. Rost, *Nanotechnology*, **24**, 365701 (2013).
- ²⁴G. J. Verbiest, T. H. Oosterkamp, and M. J. Rost, *Nanotechnology*, **28**, 085704 (2017).
- ²⁵G. S. Shekhawat and V. P. Dravid, *Science*, **310**, 89 (2005).
- ²⁶H. J. Sharahi, G. S. Shekhawat, V. Dravid et al., *Nanoscale*, **9**, 2330 (2017).
- ²⁷T. Tsuji, and K. Yamanaka, *Nanotechnology*, **12**, 301 (2001).
- ²⁸A. F. Sarioglu, A. Atalar, and F. L. Degertekin, *Appl. Phys. Lett.*, **84**, 5368 (2004).
- ²⁹Z. Parlak and F. L. Degertekin, *J. Appl. Phys.*, **103**, 114910 (2008).
- ³⁰J. P. Killgore, J. Y. Kelly, C. M. Stafford, M. J. Fasolka, and D. C. Hurley, *Nanotechnology*, **22**, 175706 (2011).
- ³¹M. Hennes, A. M. Jakob, F. Lehnert et al., *Nanoscale*, **8**, 9398 (2016).
- ³²M. J. Cadena, Y. Chen, R. G. Reifengerger, and A. Raman, *Appl. Phys. Lett.*, **110**, 123108 (2017).
- ³³F. Dinelli, P. Pingue, N. D. Kay, and O. V. Kolosov, *Nanotechnology*, **28**, 085706 (2017).
- ³⁴A. Yao, K. Kobayashi, S. Nosaka, K. Kimura, and H. Yamada, *Sci. Rep.*, **7**, 42718 (2017).
- ³⁵K. Kimura, K. Kobayashi, K. Matsushige, and H. Yamada, *Ultramicroscopy*, **133**, 41 (2013).
- ³⁶C. Ma, Y. Chen, W. Arnold, and J. Chu, *J. Appl. Phys.*, **121**, 154301 (2017).
- ³⁷U. Rabe, M. Kopycinska-Müller, and S. Hirsekorn, in *Acoustic Scanning Probe Microscopy*, edited by F. Marinello, D. Passeri, and E. Savio, (Springer, Berlin, Heidelberg, 2013), pp. 123153.
- ³⁸E. Kester, U. Rabe, L. Presmanes, P. Tailhades, and W. Arnold, *J. Phys. Chem. Solids*, **61**, 1275 (2000).
- ³⁹D. C. Hurley, M. Kopycinska-Müller, A. B. Kos, and R. H. Geiss, *Meas. Sci. Technol.*, **16**, 2167 (2005).
- ⁴⁰H. Wagner, D. Bedorf, S. Küchemann et al., *Nat. Mater.*, **10**, 439 (2011).
- ⁴¹J. P. Killgore and F. W. DelRio, *Macromolecules*, **51**, 6977 (2018).
- ⁴²J. A. Turner, and J. S. Wiehn, *Nanotechnology*, **12**, 322 (2001).
- ⁴³A. Perriot and E. Barthel, *J. Mater. Res.*, **19**, 600 (2004).
- ⁴⁴R. Szilard, *Theories and Applications of Plate Analysis: Classical Numerical and Engineering Methods*, (John Wiley Sons, Inc., Hoboken, New Jersey, 2004), pp. 161165.
- ⁴⁵P. A. Yuya, D. C. Hurley, and J. A. Turner, *J. Appl. Phys.*, **109**, 113528 (2011).
- ⁴⁶C. Ma, Y. Chen, and T. Wang, *AIP Adv.*, **5**, 027116 (2015).
- ⁴⁷S. Park, H. C. Floresca, Y. Suh, and M. J. Kim, *Carbon*, **48**, 797 (2010).
- ⁴⁸K. Kim, Z. Lee, W. Regan et al., *ACS Nano*, **5**, 2142 (2011).
- ⁴⁹Y. V. Lange, *Nondestruct. Test. Eval.*, **11**, 177 (1994).
- ⁵⁰I. I. Argatov, *J. Mech. Phys. Solids*, **70**, 190 (2014).
- ⁵¹W. Zhang, Y. Chen, H. Liu, and L. Zheng, *Appl. Phys. Lett.*, **113**, 193105 (2018).